Transformer Volume Reduction: A New Analysis and Design of an SSSA Control Based 20kW High Power Density Wide Range Resonant Converter

Shi, Zhe; Tang, Yu; Zhang, Zhe; Ge, Leijiao; Davari, Pooya

Transformer Volume Reduction: A New Analysis and Design of an SSSA Control Based 20kW High Power Density Wide Range Resonant Converter

Zhe Shi, Yu Tang, *Senior Member, IEEE,* Zhe Zhang*, Senior Member, IEEE,* Leijiao Ge*, Senior Member, IEEE*, and Pooya Davari, *Senior Member, IEEE*

Abstract—**Isolated DC/DC converters play a pivotal role in the realm of power electronics, particularly in the context of electric vehicle (EV) fast charging. These converters are responsible for delivering high-voltage direct current to EVs, sourced from a 3-phase power factor correction (PFC) converter, and exhibit compatibility with both low-voltage and high-voltage vehicle batteries. However, in many instances, the demand for constant power charging in various applications results in a significant portion of the transformer volume, thereby leading to a decrease in converter power density. This paper presents a new analysis and design for a converter based on secondary side semi-active (SSSA) control. This analysis provides theoretical support for transformer volume reduction and power density increase. It employs SSSA control to transfer stored energy from the transformer to the resonant network during boost operation, even when $f_s > f_r$, with the excitation inductance participating in resonance. Based on this analysis, the design of a 20kW 650-850V input to 300-900V with 66.7A max output prototype is discussed. The objective is to achieve the highest feasible converter power density. The designed results confirm that the 2*PQ6535 (or 1*PQ6549) core can effectively serve the 20kW transformer, resulting in an ultra-high power density of 14.36 kW/L (235 W/in3).**

Index Terms—**Transformer volume reduction, secondary side semi-active (SSSA), high power density, voltage range.**

I. INTRODUCTION

Designing a high power density DC/DC converter is an eternal goal for all workers. Among all the applications, the high power density converter design used for the EV fast charging application was the most difficult. Different from converters in other applications (realized the maximum output power at its maximum output voltage), converters in EV fast charging applications need to achieve constant power charging under all output voltage ranges. Thus, it enhances the design difficulty of that type of converter, especially for the transformer. Transformers must undertake the transmission of all converter power while meeting the converter maximum

voltage and current requirements. This will lead to a large transformer volume. Some research indicates that transformers occupy more than 20% of the converter's total volume[1-2]. Thus, research on transformer reduction methods is the main issue in achieving the converter goal of high power density design.

Discussing the transformer volume reduction method cannot be done regardless of the converter topology selection. In the field of EV fast charging, resonant and phase-shift are the main topology selection types due to soft switching, such as LLC and phase-shift full-bridge (PSFB). Compared to the phase-shift type topology, the resonant type can achieve all soft switching in a wider constant power voltage range, making it the most widely used selection. However, in this application, the transformer volume of the resonant type topology is quite large, especially for LLC. Researchers have conducted many positive explorations on this issue, including, but not limited to: customized cores[3], magnetic integration[4], magnetic coupling[5] and planar transformer with printed circuit board (PCB) winding[6-7]. These methods reduced the transformer volume to a certain extent and improved the converter power density. However, the effect is limited because this issue remains unsolved at the root. Based on the transformer equation of $A_e * N * B_{max} = E/4/f_s$, a resonant type topology such as LLC needs to reduce the switching frequency f_s to raise the output voltage. In this case, the increase in factor ($E/4/f_s$) increased the transformer volume-related factor ($A_e * N * B_{max}$). Thus, the pulse frequency modulation (PFM) control method was the root cause of the large transformer volume in resonant type topology such as LLC[8].

An interesting alternative to the traditionally used PFM control is secondary-side phase-shift control known as SSSA [9]. This SSSA control provides a boost operation while maintaining a fixed switching frequency for the resonant converters. For frequency range reduction, variations of this control method have been proposed in [8] and [10]. However, the deployment of this control method for transformer volume reduction remains unexplored, where increasing the switching frequency in boost mode can be harmful to power density requirements. For the SSSA control working mode analysis, variable equations have been provided in [8-10] and [11-12].

However, the length of the variable equation may exceed a few pages, and numerical results can only be calculated by mathematical software. To address all the above mentioned problems, this paper provides a new analysis, design, and comprehensive evaluation of this SSSA control-based converter with the aim of realizing transformer volume reduction and increased converter power density.

Compared with the previous work, the new contributions in this paper are as follows:

1. Indicate the effect and inherent mechanism of the SSSA method on transformer volume reduction. Further increased the boundary of the transformer volume limitation.

2. The linearized analysis of the SSSA control-based converter simplified the converter variable expressions. Based on the converter parameters and working conditions, all converter variables have numerical results, which facilitates the use of automation and artificial intelligence (AI) software for hardware design.

3. A new converter design that comprehensively shows the advantages and disadvantages of the SSSA control-based resonant converter.

II. CONVERTER ANALYSIS

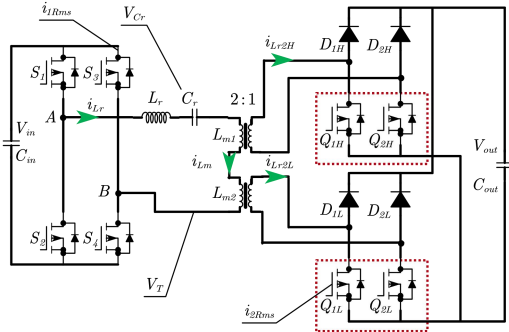### A. Converter Working Principle Analysis

Fig. 1. SSSA control-based resonant converter topology.

Fig. 1 shows the topology of the SSSA controlled resonant converter. It includes: a high-frequency inverter H-bridge composed of S_1-S_4; two semi-active controlled rectifier H-bridges composed of diode $D_{1\text{-}2HL}$ and switch $Q_{1\text{-}2HL}$; and a resonant network composed of L_r, C_r, L_m. The transformer consists of two matrix transformers with a turn ratio of 1:1. The primary side of the matrix transformer is connected in series, and the secondary side is connected to two semi-controlled rectifier bridges. Therefore, the equivalent turn ratio of the transformer n is 2:1, L_m=L_{m1}+L_{m2}.

The converter adopts fixed frequency SSSA control. SSSA adjusts the output voltage by adjusting the phase shift angle D_s of the rectifier bridge switch Q_{1HL}-Q_{2HL} relative to S_1-S_2. The larger the D_s, the higher the output voltage, as shown in Fig. 2.

Ignoring the dead time t_{dead}, we divide the working waveform of the converter within half cycle into 3 modes, The duration of the 3 modes is T_1, T_2, and T_3. Then we drew the equivalent circuit diagrams of the 3 modes as shown in Fig. 3.
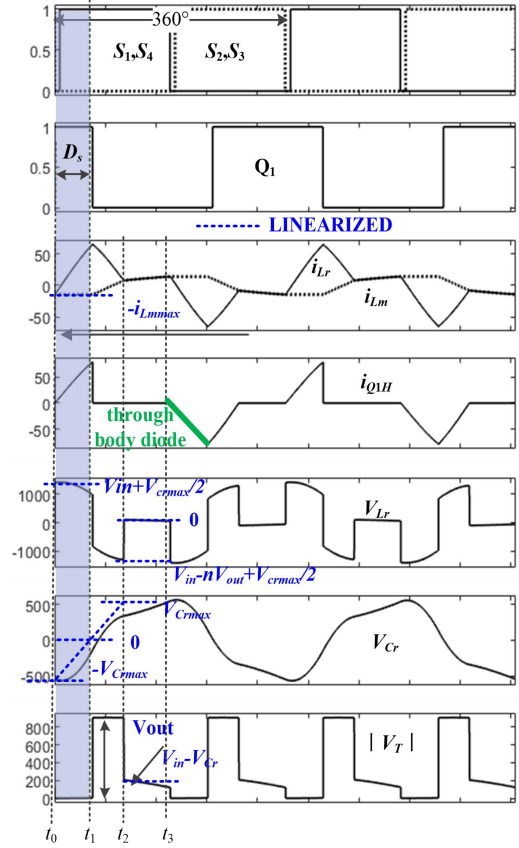

Fig. 2. SSSA control-based resonant converter key working waveforms.

1) Short-circuit mode 1[t_0 - t_1]. Within this time, the driving signals of S_1, S_4, and Q_1 are high. The secondary side resonant current i_{Lr2} passes through Q_1 and the body diodes of Q_2 to short-circuit the transformer secondary side winding. Therefore, the transformer voltage V_T on the primary side is 0. At this time, the input power will charge the resonant network. The resonant network begins to store energy, and the resonant current i_{Lr} increase linearly. Based on this, we linearized the circuit, as shown by the blue dashed line in Fig. 2. Then, we obtained the time-domain expressions for each variable (1).

$$\begin{cases} V_{Lm} = 0 \\ V_{Cr} = -V_{Cr\max}/2 \\ V_{Lr} = V_{in} - V_{Cr} \end{cases} \rightarrow \begin{cases} i_{Lm}(t) = -i_{Lm\max} \\ i_{Lr}(t) = -i_{Lm\max} + \dfrac{V_{Lr}}{L_r} \times t \end{cases} \quad (1)$$

2) L_r/C_r resonant mode 2[t_1 - t_2]. Within this time, the driving signals of S_1, S_4, and Q_2 are high, and the transformer winding is no longer short-circuited. L_r will resonate with C_r. The energy stored in the last mode with the input power is transferred together to the load. Based on that, we obtain:

$$\begin{cases} V_{Lm} = nV_{out} \\ V_{Cr} = V_{Cr\max}/2 \\ V_{Lr} = V_{in} - V_{Lm} - V_{Cr} \end{cases} \rightarrow \begin{cases} i_{Lm}(t) = -i_{Lm\max} + \dfrac{V_{Lm}}{L_m} \times t \\ i_{Lr}(t) = i_{Lr\max} + \dfrac{V_{Lr}}{L_r} \times t \end{cases} \quad (2)$$
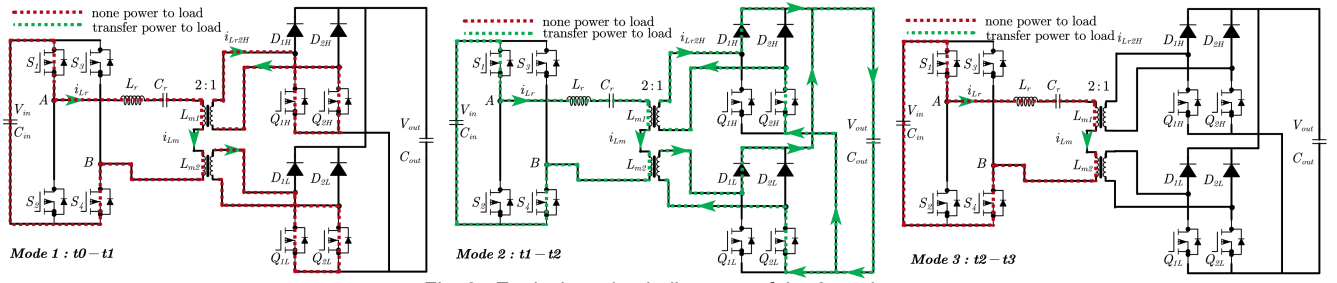
Fig. 3. Equivalent circuit diagrams of the 3 modes.

3) $L_r/C_r/L_m$ resonant mode 3[t_2 - t_3]. Within this time, the driving signals are the same as those in the previous mode. However, the resonant current i_{Lr} decreases to i_{Lm}, so there is a three-element resonance of $L_r/C_r/L_m$. Based on that, we obtain:

$$\begin{cases} V_{Lm} = V_{in} - V_{Cr} \\ V_{Cr} = V_{Cr\,max} \\ V_{Lr} = 0 \end{cases} \rightarrow \begin{cases} i_{Lm}(t) = i_{Lm}(t_2) + \dfrac{V_{Lm}}{L_m} \times t \\ \\ i_{Lr}(t) = i_{Lm}(t_2) + \dfrac{V_{Lm}}{L_m} \times t \end{cases} \quad (3)$$

Based on the above analysis, we know that only mode 2 can transfer power to the load. Thus, we obtain:

$$\begin{cases} \displaystyle\int_{t_1}^{t_2} i_{Lr2\,max}\,dt = \frac{1}{2} I_{out} \rightarrow \int_{t_1}^{t_2} n\Delta i_{Lr}\,dt = \frac{1}{2} I_{out} \\ \\ i_{Lr2H\,max} = \Delta i_{Lr} = \dfrac{V_{out}T_s}{nRT_2} \\ \\ i_{Lr2H\,max} = \Delta i_{Lr} = i_{Lr\,max} + i_{Lm\,max} \end{cases} \quad (4)$$

Based on (2), (3), (4), we can get the duration of mode 2 T_2:

$$\begin{cases} T_2 = \sqrt{\dfrac{L_r L_m V_{out} T_s}{n^2 L_r V_{out} R + n L_m R(n V_{out} + V_{Cr\,max}/2 - V_{in})}} \\ \\ V_{Cr\,max} = \dfrac{\sqrt{2}\,i_{Lrrms}}{2\pi f_s C_r} \\ \\ i_{Lrrms} = \sqrt{i_{in}^2 + i_{Lmrms}^2},\ i_{in} = \dfrac{P_{in}}{V_{in}},\ i_{Lmrms} = \dfrac{V_{in}}{2\pi f_s L_m} \end{cases} \quad (5)$$

Combined (2), (3), (4) and (5), we can get:

$$\begin{cases} T_1 = D_s T_s = \dfrac{L_r V_{out} T_s}{nRT_2(V_{in} + V_{Cr\,max}/2)} \\ \\ T_3 = \dfrac{T_s}{2} - T_1 - T_2 \\ \\ i_{Lm\,max} = \dfrac{n V_{out} T_2 + (V_{in} + V_{Cr\,max})T_3}{2L_m} \\ \\ i_{Lr\,max} = i_{Lr2H\,max} - i_{Lm\,max} = \Delta i_{Lr} - i_{Lm\,max} \\ \qquad\quad = \dfrac{V_{out}T_s}{2RT_2} - \dfrac{n V_{out} T_2 + (V_{in} + V_{Cr\,max})T_3}{2L_m} \end{cases} \quad (6)$$

Thus, if we know the converter parameter values of (L_r, C_r, L_m) and the working conditions of (V_{in}, V_{out}, n, P_{out}, R, f_s), then we can obtain all the variable values in the converter of (V_{Crmax}, V_{Crrms}, i_{Lrrms}, i_{Lrmax}, $i_{Lr2Hrms}$, i_{Lmrms}, i_{Lmmax}, D_s, T_1, T_2, T_3) for all the converter component hardware designs.

Also, based on the converter variable equations and working conditions, we can use that for converter parameter design.

B. Converter Characteristics Analysis

From the above analysis, we already know the value of each variable and the duration of the 3 modes. Combined with equation(5) and (6), we obtain the relationship between the output voltage V_{out} and the phase shift angle D_s, as shown in equation (7). From this, we know that the output voltage V_{out} is positively correlated with D_s. In addition, it was positively correlated with the duration T_1 of mode 1. This is the same as the results of the circuit modal analysis: the longer the T_1 time, the longer the transformer winding short-circuited time, the higher the resonant network energy stored, and thus the higher the output voltage.

$$V_{out} = D_s \times \frac{2RT_2(V_{in} + V_{Cr\,max}/2)}{L_r V_{out} T_s} \quad (7)$$

Except for the converter voltage gain characteristics, another converter focus characteristic is soft switching. For the ZVS-ON of S_1-S_4, S_1-S_4 needs to have a negative resonant current after the dead time to maintain the device drain-source voltage at 0, which must meet the requirements of (8). For the ZVS-ON of Q_1-Q_2, due to the presence of short-circuit mode 1, Q_1-Q_2 will always be operated by another switch to short-circuit the transformer winding before turning-on, causing the body diode to continue flowing. Therefore, Q_1 and Q_2 are unconditional ZVS-ON.

$$-i_{Lm\,max} + \frac{V_{in} + V_{Cr\,max}/2}{L_r} \times t_{dead} < 0 \quad (8)$$

For D_1-D_2, the key to achieving ZCS-OFF is that the current flowing through the diode naturally reduces to 0, which requires the excitation inductance L_m to participate in resonance, thus requiring a duration T_3 >0 for mode 3.

$$\begin{cases} \dfrac{T_s}{2} - T_1 - T_2 > 0 \end{cases} \quad (9)$$

III. TRANSFORMER STRESS ANALYSIS

To evaluate the transformer stress (transformer maximal magnetic field intensity B_{Tmax}), there are generally 2 commonly used methods as (10): transformer average voltage E_{Tavg} based

equation and transformer maximal excitation current i_{Lmmax} based equation.
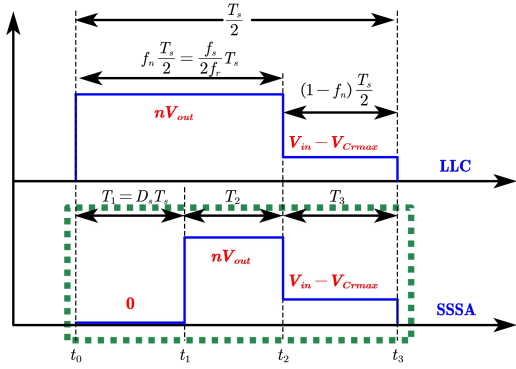

Fig. 4. Transformer voltage of 2 topologies.

Here, for easy understanding, we use E_{Tavg} based equation to evaluate the transformer stress B_{Tmax} and make 2 topologies of LLC and SSSA into comparison, as shown in Fig. 4. Fig. 4 shows that the SSSA achieves boost operation with the participation of mode 1, and the transformer voltage was always 0 within mode 1 duration time T_1. Thus, the E_{Tavg} of SSSA is much smaller than that of LLC. Besides, because mode 3 existed in SSSA, L_m participated in resonance, E_{Tavg} of SSSA can be reduced more, even $f_s > f_r$. Combined with the control method of these 2 topologies, LLC needs to reduce f_s to achieve boost operation, but the f_s of SSSA is fixed. Thus, the B_{Tmax} of SSSA will be further reduced. This is the basic principle by which the SSSA control-based converter can reduce the transformer volume size.

$$\begin{cases} B_{T\max} = \dfrac{E_{Tavg}}{4 f_s A_e N} \\ B_{T\max} = \dfrac{i_{Lm\max} L_m}{A_e N} \end{cases} \tag{10}$$

$$\begin{cases} E_{Tavg}(LLC) = \displaystyle\int_0^{T_s/2} E_T dt \\ = \dfrac{nV_{out} f_n T_s + (1 - f_n)(V_{in} - V_{Cr\max})}{2} \\ E_{Tavg}(SSSA) = \displaystyle\int_0^{T_s/2} E_T dt \\ = \dfrac{2}{T_s}(T_2 nV_{out} + T_3(V_{in} - V_{Cr\max})) \end{cases} \tag{11}$$

Based on the above analysis, we obtain E_{Tavg} equation (11) for these 2 topologies. Moreover, we made the 2 topologies transformer average voltage curves under a wide output voltage range from 300V to 900V, as shown in Fig. 5. From Fig. 5, it can be seen that the maximum E_{Tavg} =1260V of LLC is much larger than the E_{Tavg} =639V of SSSA at the maximum output voltage of 900V. At this point, considering different switching frequencies, the transformer stress of the SSSA is only 21.6% of LLC. Thus, SSSA can use a smaller transformer magnetic core or only 21.6% transformer winding turns than the LLC transformer to reduce the transformer volume size. This is consistent with our theoretical analysis.

$$\begin{cases} E_{Tavg}(\max) = nV_{out} = V_{in} \times M_{AC} \\ M_{AC} = \dfrac{1}{n\sqrt{(1 + k - \dfrac{k}{f_n^2})^2 + Q^2(f_n - \dfrac{1}{f_n})^2}} \\ k = \dfrac{L_r}{L_m}, Q = \dfrac{\sqrt{L_r / C_r}}{R_{ac}}, n = \dfrac{n_p}{n_s}, \\ f_n = \dfrac{f_s}{f_r}, R_{ac} = \dfrac{8}{\pi^2} R n^2 \end{cases} \tag{12}$$
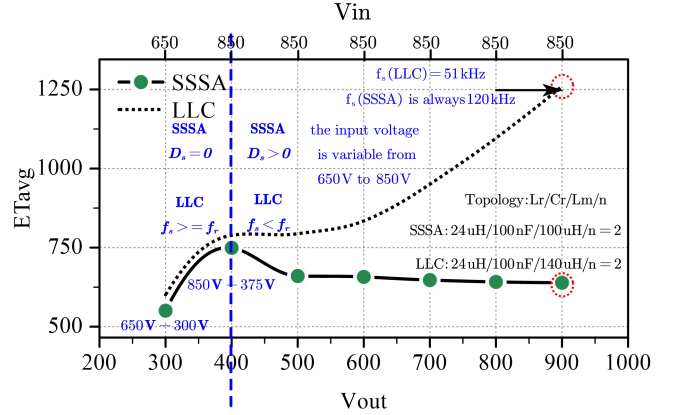

Fig. 5. 2 topologies transformer average voltage curves under a wide output voltage range.

However, the E_{Tavg} curve of the SSSA is not flat, and the maximum E_{Tavg} of the SSSA occurs at the 375V output voltage point. Based on equation (11), we can get the SSSA maximum E_{Tavg} equation (12). From this, we know that the SSSA maximum E_{Tavg} occurs at the highest input voltage V_{in} of 850V and minimum phase shift angle D_s of 0 with an output voltage of 375V. Considering that high-power DC/DC often uses variable bus voltage control[9], the input voltage varies between 650V and 850V. We can increase f_s or decrease V_{in} to make the SSSA E_{Tavg} curve flat and reduce the maximum value of E_{Tavg}.

Here, based on the above analysis, finite element analysis (FEA) simulations were conducted for the matrix transformer of these two topologies. The parameters and results of the FEA simulations are shown in Fig. 6. The rated power for both topologies in the simulations was 10kW, and each transformer of the topology consisted of two matrix transformers connected in series. The matrix transformer for the SSSA topology utilized a PQ6535 magnetic core, while the LLC topology employed a PQ6562 magnetic core. From the FEA simulation results, it can be observed that the B_{Tmax} of the LLC topology is higher than that of the SSSA topology. However, considering the different switching frequencies and effective duty cycles of the two topologies, the proportional core loss per unit volume (Pcv) for the magnetic cores of both topology transformers is the same. It should be noticed that, in achieving the functionality of a 20 kW transformer, the SSSA topology used a smaller magnetic core (36.3% of the LLC) and fewer winding turns (36.4% of the LLC), resulting in lower transformer losses (43.1% of the LLC) and power density.
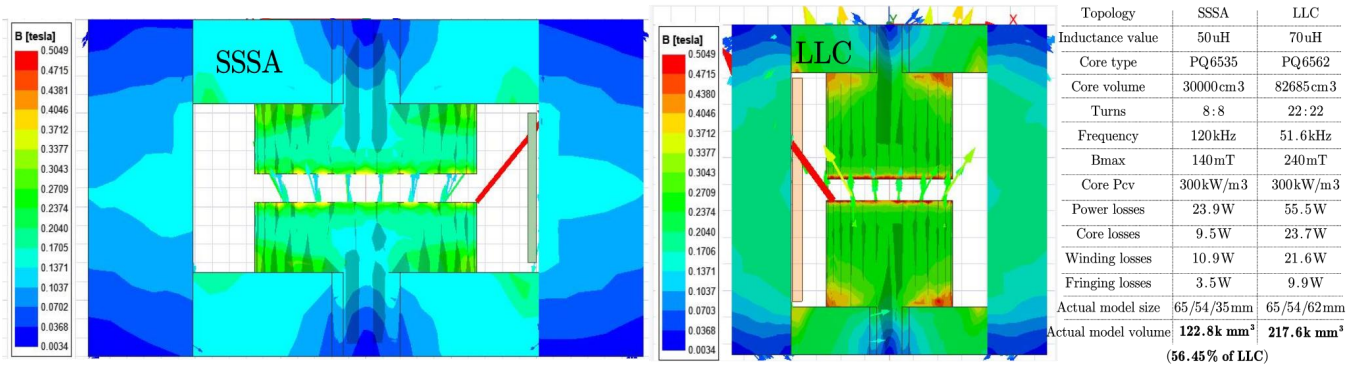
Topology	SSSA	LLC
Inductance value	50 uH	70 uH
Core type	PQ6535	PQ6562
Core volume	30000 cm3	82685 cm3
Turns	8:8	22:22
Frequency	120kHz	51.6kHz
Bmax	140mT	240mT
Core Pcv	300kW/m3	300kW/m3
Power losses	23.9W	55.5W
Core losses	9.5W	23.7W
Winding losses	10.9W	21.6W
Fringing losses	3.5W	9.9W
Actual model size	65/54/35mm	65/54/62mm
Actual model volume	**122.8k mm³**	**217.6k mm³**
		(56.45% of LLC)

Fig. 6. The results and parameters of two topology FEA simulations, at V_{out}=900V.

IV. DESIGN CONSIDERATIONS

The design considerations are based on EV fast charging applications. Thus, this SSSA control-based resonant converter should achieve a constant 20kW power operation at an output voltage range of 300V-900V with a variable input voltage range of 650V-850V.

A. Switching and Resonant Frequency

The switching and resonant frequencies were mainly determined by:

1. Convenience of comparison: most papers and industrial products choose a 100kHz resonant frequency.

2. Magnetic core materials of the transformers and inductors: the most suitable magnetic material for this application is PC95, which has a best working frequency range of 100-200kHz.

3. Limitation of the semiconductor devices: with this converter voltage level, all switches are selected with SiC devices. Because all switches Q_{1-2} on the secondary side turn off at the maximum current point, as shown in Fig. 2 i_{Q1H}. Therefore, for the turning-off loss concern, the switching frequency should be as low as possible.

4. Transformer maximum E_{Tavg}: we can increase a little f_s to reduce the transformer stress based on (12).

Therefore, we chose the converter switching and resonant frequency to be around 100kHz.

B. Transformer

The transformer volume size depended on its maximum voltage stress (B_{Tmax}, E_{Tavg}) and transformer utilization rate across all output voltage ranges. Based on Fig. 5, we know that the larger the SSSA control range, the flatter E_{Tavg} curve, and the higher the transformer utilization rate. To maximize the superiority of the SSSA control method in reducing the transformer volume size, we allowed the converter to use SSSA control across all output voltage ranges. This means that D_s=0, and the converter rated output voltage at the lowest input voltage V_{in}=650V is 300V. Based on equation (12), we know that increasing the switching frequency f_s can reduce the maximum transformer stress. Based on these considerations, we can determine that the transformer turn ratio is 2:1 and the specific switching frequency f_s is 120kHz.

Another transformer design consideration is the winding. If the wire diameters (winding current density) of the transformer primary and secondary windings are similar, the transformer winding space utilization rate is higher. Considering the converter primary and secondary voltage range, converter all components height, and rectifier H-bridge current value, we choose to use two pairs of 1:1 transformers to form a matrix transformer.

Therefore, the magnetic core selection for these two transformers is PC95-PQ6535. According to equation (5), the winding RMS current value can be calculated, and the winding wire is selected as 0.1*550 litz wire. According to equation (10), the transformer winding turns can be calculated as 2*8:8. The B_{Tmax} is 163.4mT at V_{out}=375V, B_{Tmax} is 139.3mT at V_{out}=900V. The excitation inductance L_m value is 100uH, calculated by (8).

In addition, the transformer can be replaced by a single 16:8:8 turns PQ6549 transformer with the same 0.1*550 winding wires.

To evaluate the transformer power losses, we can use:

$$\begin{cases} P_{loss\_T} = P_{T\_loss\_core} + P_{T\_loss\_winding} + P_{T\_loss\_fringing} \\ P_{T\_loss\_core} = P_{cv}V_e = kf_s^{\alpha}B_{T\max}^{\beta}\dfrac{8^{a-1}D^{1-a}}{\pi^{2(a-1)}} \\ P_{T\_loss\_winding} = (i_{Lrrms}^2 + i_{Lr2rms}^2)R_{winding} \\ P_{T\_loss\_fringing} = 4.896\times10^{-4}l_g l_d B_{T\max}^2 f_s^2 \end{cases} \quad (13)$$

C. Resonant Components

The resonant components include resonant inductors and capacitors. According to equation (6), the larger the resonant inductance value L_r, the smaller the resonant peak current i_{Lrmax}, the resonant inductance magnetic core stress B_{Lrmax}, and the inductor power losses. When the resonant frequency is fixed, we need to keep the resonant capacitor value C_r as small as possible to obtain a large resonant inductance value L_r.

The resonant capacitor value selection mainly considers the capacitor AC withstand voltage (leave a certain margin based on the highest operating temperature) and material-frequency characteristics. Thus, we choose a 105nF C_r value made by 7 high frequency material (MMKP82 650VAC 15nF) capacitors in parallel. The withstand voltage of this material at 105 degrees is 386V, which is just greater than the V_{Crrms} 330V calculated by equation (5). Based on the 100kHz resonant frequency, the resonant inductance value L_r should be approximately 24uH.

For higher power density considerations of the converter , all components should be of the same height. Thus, we chose PQ3535 as the resonant inductance magnetic core. The winding selection of the inductor is the same as that of the transformer winding, which is 0.1*550 litz wire. Based on the space in the

PCB layout process, we can use 4 6uH PQ3535 (with winding turns of 12) inductors in series to form the 24uH resonant inductor. And the maximum inductance stress B_{Lrmax} is 190.7mT, the i_{Lrmax} was calculated by (6), and the B_{Lrmax} was calculated by (14). Equation (15) can be used to evaluate the resonant inductor power losses.

Here, we completed the design process, and the entire resonant parameter design flowchart is shown in Fig. 7. The design sequence of the design flowchart is consistent with the design consideration discussion sequence.

$$B_{Lr\max} = \frac{i_{Lr\max} L_r}{A_e N} \tag{14}$$

$$\begin{cases} P_{loss\_Lr} = P_{Lr\_loss\_core} + P_{Lr\_loss\_winding} + P_{Lr\_loss\_fringing} \\ P_{Lr\_loss\_core} = P_{cv} V_e = k f_s^\alpha B_{Lr\max}^\beta \frac{8^{a-1} D^{1-a}}{\pi^{2(a-1)}} \\ P_{Lr\_loss\_winding} = i_{Lrrms}^2 R_{winding} \\ P_{Lr\_loss\_fringing} = 4.896 \times 10^{-4} l_g l_d B_{Lr\max}^2 f_s^2 \end{cases} \tag{15}$$

```
┌─────────────────────────────────┐
│           f_s / f_r             │
├─────────────────────────────────┤
│ voltage gain      equation(8)   │
│        ↓                        │
├─────────────────────────────────┤
│   L_m /transformer turn tatio n │
├─────────────────────────────────┤
│ C_r withstand voltage  equation(5) │
│        ↓                        │
├─────────────────────────────────┤
│           C_r                   │
├─────────────────────────────────┤
│ f_r resonant frequency  equation(14) │
│        ↓                        │
├─────────────────────────────────┤
│           L_r                   │
└─────────────────────────────────┘
```
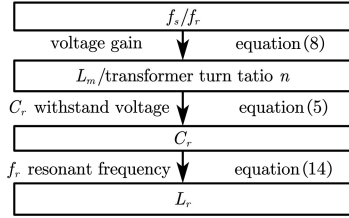
Fig. 7. Resonant parameter design process.

D. Switching Devices

According to the converter working voltage level, all the switching devices and rectifier diodes should use 1200V SiC devices. The converter circuit current reaches its maximum at a minimum output voltage of 300V. At that time, D_s=0, S_{1-4} and Q_{1-2} continuous drain current should be above the primary and secondary maximal RMS currents $i_{1rmsmax}$ and $i_{2rmsmax}$. As for the diodes D_{1-2}, continuous rectified forward current should be above the secondary maximal average current $i_{2upavgmax}$. Thus we choose UF3C120040K4S (1200V 40mΩ) as S_{1-4} and Q_{1-2}. For device convenience, we choose the body diode of UF3C120040K4S as D_{1-2}, its forward voltage V_F=1.5V was small as normal SiC diodes.

$$\begin{cases} i_{1rms\max} = \sqrt{2} \frac{P_{out}}{V_{out}} \frac{1}{4} \\ i_{2downrms\max} = \sqrt{2} \frac{P_{in}}{V_{out}} \frac{1}{4} \\ i_{2upavg\max} = \frac{P_{out}}{V_{out}} \frac{1}{4} \end{cases} \tag{16}$$

Considering the SSSA control method, the converter has maximal power losses at the maximum output voltage point due to the turning-off losses. Equation (17) can be used to evaluate the device power losses at this point. Since the UF3C120040K4S (cascode) used in this paper and the reverse current flow through the cascode devices should be considered as through a si-body-diode and a sic-fet in series. The power loss equation (17) should be revised to (18).

$$\begin{cases} P_{S1-4} = i_{1rms}^2 R_{ds} + f_s E_{off\_e} = \frac{i_{Lr2H}}{2\sqrt{3}}^2 R_{ds} + f_s \frac{i_{Lm\max} V_{in}}{i_{off} V_{off}} \\ P_{D1-2} = V_F i_{2upavg} = V_F \frac{P_{out}}{V_{out}} \frac{1}{4} \\ P_{Q1-2} = P_{Q1-2}(rds) + P_{Q1-2}(V_F) + P_{Q1-2}(turn-off) \\ P_{Q1-2}(rds) = i_{2rms}^2 R_{ds} = \frac{i_{Lr2H}}{2\sqrt{3}}^2 R_{ds} \\ P_{Q1-2}(V_F) = V_F i_{2downavg} = V_F \frac{i_{Lr2H}}{2} D_s \\ P_{Q1-2}(turn-off) = f_s E_{off\_e} = f_s E_{off} \frac{i_{Lr2H} V_{out}}{i_{off} V_{off}} \end{cases} \tag{17}$$

$$\begin{cases} P_{D1-2} = V_F i_{2upavg} + i_{2uprms}^2 R_{ds} = V_F \frac{P_{out}}{V_{out}} \frac{1}{4} + i_{2uprms}^2 R_{ds} \\ P_{Q1-2} = P_{Q1-2}(rds) + P_{Q1-2}(V_F) + P_{Q1-2}(turn-off) \\ P_{Q1-2}(rds) = i_{2rms}^2 R_{ds} = \frac{i_{Lr2H}}{2\sqrt{3}}^2 R_{ds} \\ P_{Q1-2}(V_F) = V_F i_{2downavg} = V_F \frac{i_{Lr2H}}{2} D_s \end{cases} \tag{18}$$

V. EXPEROMENTAL VERIFICATION

To verify the converter analysis and evaluate the SSSA control-based converter performance, we built a 20kW prototype, as shown in Fig. 8. Detailed hardware parameters are shown in Table I.
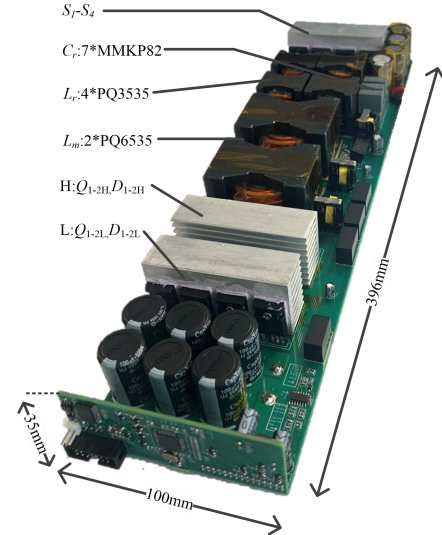

Fig. 8. 20kW SSSA control-based resonant converter prototype.

For the converter ZVS concern, based on equation (8), we know that a high di_{Lr}/dt was bad for S_{1-4} ZVS achievement. The converter has the highest diLr/dt when it reaches the highest output voltage. Fig. 9 shows the ZVS-ON waveforms of S_2 and Q_1 at 1000V output voltage light load (means low output power) conditions, where the dead time is 200ns. Based on this, the converter realized ZVS-ON under the most difficult working

conditions; thus, the converter will have ZVS soft switching in all other conditions.

TABLE I
DETAILED PARAMETERS OF THE HARDWARE

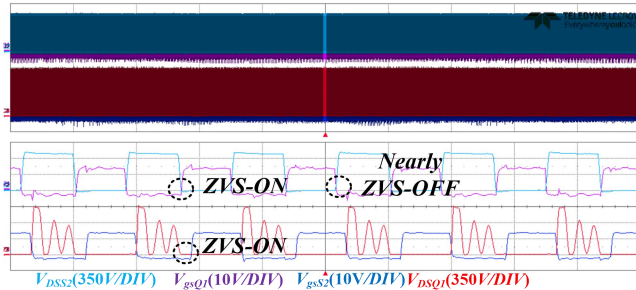| Parameter	Value	Parameter	Value
f_r	102kHz	S_{1-4}	UF3C120040K4S
f_r	120kHz	Q_{1-2}	UF3C120040K4S
L_r	24uH	D_{1-2}	UF3C120040K4S
C_r	105nF	V_{in}	650-850V
L_m	100uH	V_{out}	300-900V
$n_p : n_s$	16:8:8	P_{out}	20kW
L*W*H:398*100*35mm		Power density：14.36kW/L	
Realized 20kW working power at all output voltage range, with a maximum output current of 66.7A			

Fig. 9. ZVS realization waveform: V_{in} = 850V, V_{out} = 1000V P_{out} = 1.3 kW, at f_s = 120kHz.
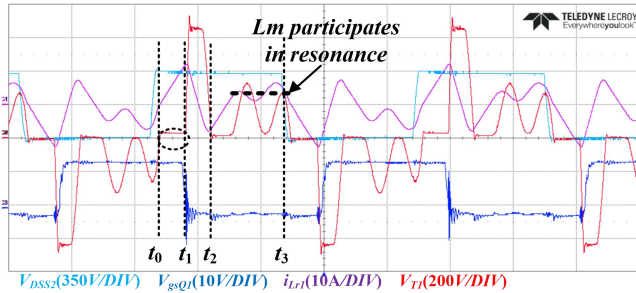

Fig. 10. $V_T/i_{Lr}/V_{DSS2}/V_{gsQ2}$ waveform: V_{in} = 700V, V_{out} = 700V P_{out} = 1.3 kW, at f_s = 120kHz.
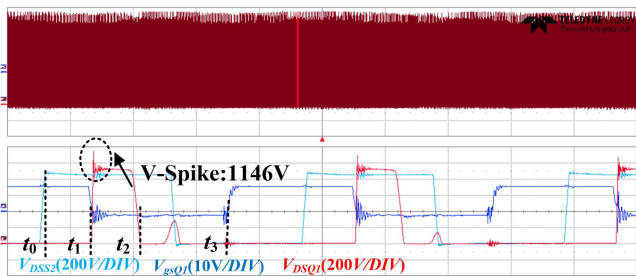

Fig. 11. $V_{DSS2}/V_{DSQ2}/V_{gsQ1}$ waveform: V_{in} = 850V, V_{out} = 900V P_{out} = 20.7 kW, at f_s = 120kHz.

For the SSSA control-based converter, the most notable characteristic was transformer reduction. Fig. 10 shows one of the PQ6535 matrix transformer primary voltage waveforms under the 700V output condition. We can see that the transformer voltage was divided into 3 part as 3 working modes in a half cycle. In mode 1, V_{DSS2} and V_{gsQ1} overlap (S_1 and Q_1 turn on), and the transformer is short-circuited; thus, the primary transformer voltage is 0. The resonant current i_{Lr} begins to increase linearly, and the resonant network begins to store energy. When Q_1 is off, the converter is in mode 2, and the stored energy and input power are discharged to the load. Thus, i_{Lr} will decrease, and V_T is V_{out}. In mode 3, L_m begins to participate in resonance, $V_T =(V_{in}-V_{CR})/2$. Due to the parasitic parameters, V_T and i_{Lr} may experience attenuation oscillations. Since L_m participates in resonance, even in $f_s > f_r$ condition, the i_{Lr} was dis-continous, thus D_1 and D_2 will realize ZCS-OFF. The waveform of the oscilloscope is consistent with the theoretical analysis; thus, the SSSA control-based converter can achieve transformer reduction.
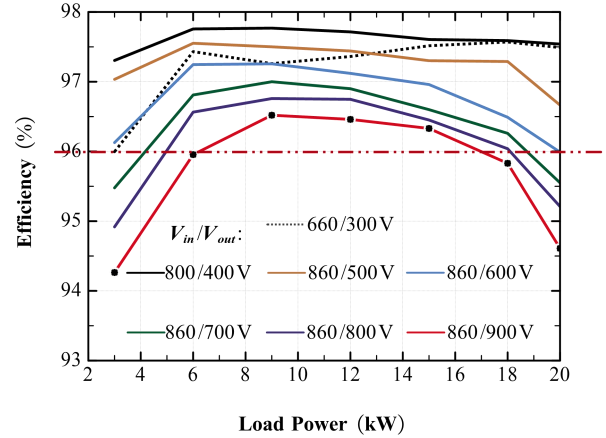

Fig. 12. Converter efficiency chart at 300-900V output voltage range.

Another thing that should be noticed is that Q_1 and Q_2 work in high current turning off states when V_{out} is above 400V. Fig. 11 shows the waveform of V_{DSQ1},when the output voltage is 900V and output power is 20.7kW. In mode 2 Q_1 off, V_{DSQ1} has a voltage spike of 1146V due to the high di_{Lr}/dt state and Q_1 drain parasitic inductance. If the di_{Lr}/dt rate was low as the Fig. 9 light load conditions, even when the output voltage V_{out} is 1000V, the V_{DSQ1} voltage spike is only 1027V.
Fig. 12 shows the converter efficiency at the 300-900V output. It can be seen that the converter maximum efficiency is 97.7% when V_{out}=400V and D_s is small (small turning-off current). As the output voltage gradually increases, the converter's full-load efficiency also gradually decreases. But most of the efficiency & V_{out} point within above 96% efficiency region. Based on the power loss equations, we can obtain the loss distribution chart at V_{out}=900V, as shown in Fig. 13. In that figure, we can see that Q_1 and Q_2 account for the majority of losses, and we can use a smaller internal resistance and a turning-off losses package (TO263-7, smd package) device to replace Q_{1-2} for efficiency improvement.

Table II shows the performance comparison of the different single-stage converters. Within that table, it can be seen that two factors can be used to evaluate transformer performance. One is the transformer score, which uses the transformer volume divided by the rated power (cm3/kW), and based on that score another score combines the switching frequency and constant power output voltage range (%). It can be seen that the converter in this paper has the wildest constant power voltage range (regardless relay), highest converter power density, and

	Type	Rated power	Topology	Constant power voltage range	Frequency	Max boost voltage gain	Transformer (cm3/kW)	Power density	Max efficiency	Score % Range/fs/(cm3/kW)
this	paper	20kW	PSM SSSA resonant	300-900V	120k	2.12	2*PQ65/35 (12.06) or 1*PQ65/49 (8.44)	14.36kW/L	97.8	69.9 or 100
[1]	reference design	30kW	PFM LLC	300-500V with relay 600-1000V	120-200k	1.28	3*PQ65/65 (30.53)	6.58kW/L	98.3	11.5
[2]	product	20kW	PFM LLC	250-500V with relay 500-1000V	70-120k	1.47	3*EI68 (30.35)	5.2kW/L	98.1	23.4
[13]	paper	6.6kW	PWM resonant	330-415V	50k	1.25	2*EE65/65 (39.35)		97.7	21.6
[14]	paper	20kW	PSM full bridge	700V	100k	1	1*EE100/20 (20)	13.3kW/L (no heatsink)		16.9
[6]	paper	6.6kW	PSM LCL-T resonant	330-500V with relay 500-950V	500k	1.9	Planar 3*EILP43 (11.29)	7.3kW/L	98.2	11.4
[7]	paper	6.6kW	CLLC	300-450V	500k	1	Planar E-core (30.29)	6.96kW/L	97.85	3.34
[15]	paper	30kW	PSM PSFB	500-682V	140k	1	4*PQ6554 (25.74)	7.2kW/L		12.8
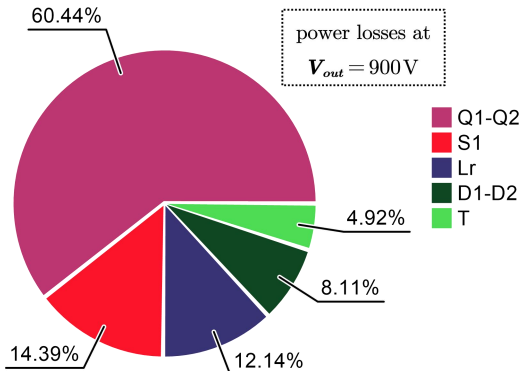
Fig. 13. Converter loss distribution chart at V_{out}=900V, full-load.

power losses at
$$V_{out} = 900 \text{V}$$

- Q1-Q2: 60.44%
- S1: 14.39%
- Lr: 12.14%
- D1-D2: 8.11%
- T: 4.92%

best transformer performance. Moreover, having an acceptable conversion efficiency even uses the highest internal resistance (r_{dson}) devices (including compared with the 6.6kW type converters).

per 10kW
Core losses: 39 W
Winding losses: 13.6 W
Fringing losses: 4.3 W
Total losses: 56.9 W
At 900V conditions

per 10kW
2 * EE65B
0.1 * 550 wire
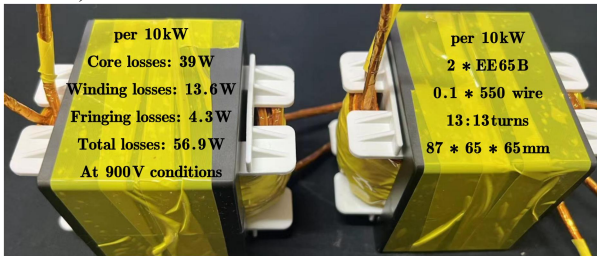13:13 turns
87 * 65 * 65 mm

Fig. 14. Transformers of the LLC prototype.

For comparison with LLC, we built an LLC prototype with the same specifications as the SSSA prototype. The LLC prototype reused the board of the SSSA, replacing only the transformer and the PFM control method. The transformer of the LLC is shown in Fig. 14, and the B_{Tmax} is 226mT. Based on this LLC prototype, we can obtain the efficiency curve and

component operating temperature of the LLC and SSSA prototypes, as shown in Fig. 15 and Table III.

V_{in}/V_{out}:

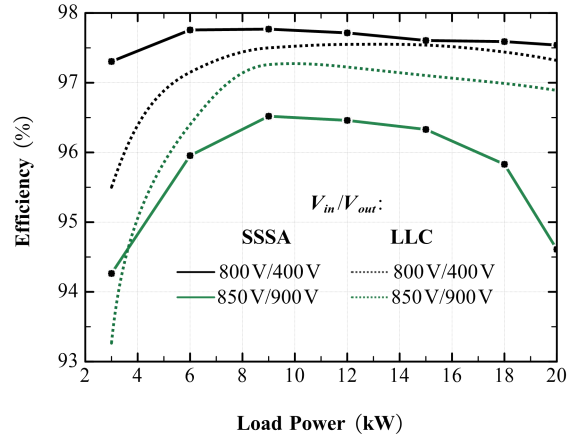|	SSSA	LLC
800 V/400 V	——	·······
850 V/900 V	——	·······

Fig. 15. A comparison of the efficiency curves of the two topologies at 400V and 900V.

Fig. 15 shows a comparison of the efficiency curves of the two topologies at 400V and 900V. 400V corresponds to the resonant frequency point of the LLC prototype, and 900V corresponds to the highest output voltage point. Fig. 15 shows that both topologies achieve high conversion efficiency at 400V, but the efficiency of the SSSA prototype is higher than that of the LLC prototype because of the lower transformer power loss of the SSSA. However, the conversion efficiency of the SSSA prototype at 900V is significantly lower than that of the LLC prototype because the semi-active rectifier bridge of the SSSA has high turning-off losses.

We used the K-type thermocouple sensor to obtain the operating temperature of two prototypes at 900V in a closed environment, as shown in Table III. After 20 minutes, the temperatures of each component cease to increase with time;

hence, the temperature values at the 20-min point can be considered as the steady-state operating temperatures for each component.

TABLE III
OPERATING TEMPERATURE OF THE LLC AND SSSA

SSSA: V_{in}=850V, V_{out}=900V, 20kW, 120kHz				
	S_4	T wingding	T core	D_2
5min, AT25	44.2	61	43.5	55.7
10min, AT27	45.1	73.5	55.8	58.1
15min, AT28.9	45.8	78.5	61.3	59.4
20min, AT29	45.8	84.6	66.5	60.6
LLC: V_{in}=850V, V_{out}=900V, 20kW, 51kHz				
5min, AT25	43.6	35.2	33	37.9
10min, AT27	51.3	48	42.4	40.2
15min, AT29	52.5	57.1	48.6	40.6
20min, AT29	53	62.4	52.1	41

5min, AT25= after operating 5 mins, and the air temperature of the cooling fan point is 25°C.

It can be seen from Table III that the temperature of the LLC transformer is lower than that of the SSSA. The core temperature of the LLC transformer is 52.1°C, which is lower than the 66.5°C of the SSSA. Because the LLC transformer volume size (87*65*65mm) is 3 times larger than that of the SSSA (65*54*35mm). The LLC transformer has a larger surface area; thus, more contact with air results in better heat dissipation. The winding temperature of the LLC transformer is 62.4°C, smaller than 84.6°C of the SSSA. One reason is the volume size, and another is the converter switching frequency. SSSA works in 120kHz, and LLC works in 51kHz. Thus, for the same winding wires (0.1*550), the proximity effect of SSSA is stronger than that of LLC.

VI. CONCLUSION

This paper presents a new analysis and design of an SSSA control-based resonant converter utilized in a wide output voltage range constant power charging DC/DC stage for EV fast charging applications. The use of SSSA control is explored to achieve transformer volume reduction. Through the converter linearized analysis, the variable equations can be easily calculated for automated design. The transformer analysis provides a theoretical basis for achieving the goal of high power density. The experimental results validate this analysis and design and fully demonstrate the advantages and disadvantages of this SSSA control-based resonant converter.

The designed prototype realized a 14.36kW/L converter power density with a wild voltage range of 300-900V and a maximum output current of 66.7A .

REFERENCES

[1] Wolfspeed, CRD30DD12N-K, Durham, North Carolina, America. [Online]. Available: https://www.wolfspeed.com/products/power/reference-designs/crd30dd12n-k/.
[2] Shijiazhuang Tonghe Electronic Technology Co., Ltd. TH20F10025C7, Shijiazhuang, Hebei, China. Aug. 2021. [Online]. Available: https://v4.cecdn.yun300.cn/100001_2102265146/%E6%96%B0%E8%8

3%BD%E6%BA%90%E4%BA%A7%E5%93%81%E6%89%8B%E5%86%8C.pdf.
[3] F. Jin, A. Nabih, Q. Li and F. C. Lee, "A Three Phase CLLC Converter with Improved Planar Integrated Transformer for Fast Charger Applications," 2021 IEEE Fourth International Conference on DC Microgrids (ICDCM), Arlington, VA, USA, 2021, pp. 1-5.
[4] Wu, M. Jiang, Z. Sun and Q. Wang, "An Internal Magnetic Core Termination Integration Method for LLC Four-Elemental Matrix Transformer," in IEEE Transactions on Power Electronics, vol. 38, no. 11, pp. 13573-13579, Nov. 2023.
[5] X. Zhang, S. Pan and P. Jain, "A Discrete Coupled Multiphase Interleaved LLC Converter With Symmetrical Components Analysis," in IEEE Transactions on Power Electronics, vol. 38, no. 11, pp. 14150-14165, Nov. 2023.
[6] S. Mukherjee, J. M. Ruiz and P. Barbosa, "A High Power Density Wide Range DC‐DC Converter for Universal Electric Vehicle Charging," in IEEE Transactions on Power Electronics, vol. 38, no. 2, pp. 1998-2012, Feb. 2023.
[7] Z. Zhang, C. Liu, M. Wang, Y. Si, Y. Liu and Q. Lei, "High-Efficiency High-Power-Density CLLC Resonant Converter With Low-Stray-Capacitance and Well-Heat-Dissipated Planar Transformer for EV On-Board Charger," in IEEE Transactions on Power Electronics, vol. 35, no. 10, pp. 10831-10851, Oct. 2020, doi: 10.1109/TPEL.2020.2980313.
[8] Y. Jang, M. M. Jovanović, J. M. Ruiz, M. Kumar and G. Liu, "Implementation of 3.3-kW GaN-based DC-DC converter for EV on-board charger with series-resonant converter that employs combination of variable-frequency and delay-time control," 2016 IEEE Applied Power Electronics Conference and Exposition (APEC), Long Beach, CA, USA, 2016, pp. 1292-1299.
[9] Z. Shi, Y. Tang, Y. Zhang, Y. Guo, H. Sun and L. Jiang, "A Secondary-Side Semiactive 3-Phase Interleaved Resonant Converter Employing Multimode Modulation Scheme for Fast EV Charger Applications," in IEEE Transactions on Power Electronics, vol. 37, no. 11, pp. 13385-13397, Nov. 2022.
[10] G. Liu, Y. Jang, M. M. Jovanović and J. Q. Zhang, "Implementation of a 3.3-kW DC‐DC Converter for EV On-Board Charger Employing the Series-Resonant Converter With Reduced-Frequency-Range Control," in IEEE Transactions on Power Electronics, vol. 32, no. 6, pp. 4168-4184, June 2017.
[11] H. Wu, T. Mu, X. Gao and Y. Xing, "A Secondary-Side Phase-Shift-Controlled LLC Resonant Converter With Reduced Conduction Loss at Normal Operation for Hold-Up Time Compensation Application," in IEEE Transactions on Power Electronics, vol. 30, no. 10, pp. 5352-5357, Oct. 2015, doi: 10.1109/TPEL.2015.2418786.
[12] X. Zhao, L. Zhang, R. Born and J. -S. Lai, "A High-Efficiency Hybrid Resonant Converter With Wide-Input Regulation for Photovoltaic Applications," in IEEE Transactions on Industrial Electronics, vol. 64, no. 5, pp. 3684-3695, May 2017.
[13] B. -K. Lee, J. -P. Kim, S. -G. Kim and J. -Y. Lee, "A PWM SRT DC/DC Converter for 6.6-kW EV Onboard Charger," in IEEE Transactions on Industrial Electronics, vol. 63, no. 2, pp. 894-902, Feb. 2016.
[14] R. Ramachandran, J. Nielsen, M. Nymand, N. Nageler and R. Eisele, "A 20 kW High Power Density Isolated DC-DC Converter for an On-board Battery Charger utilizing Very-low Inductive SiC Power Modules," 2020 IEEE Applied Power Electronics Conference and Exposition (APEC), New Orleans, LA, USA, 2020, pp. 3503-3507.
[15] D. Wang et al., "Isolated 3-Level DC‐DC Converter With Complete ZVS Using Magnetizing Inductors," in IEEE Transactions on Power Electronics, vol. 38, no. 2, pp. 1910-1923, Feb. 2023, doi: 10.1109/TPEL.2022.3212202.

Zhe Shi was born in Hebei, China, in 1994. He received the B.S. degree from the Department of Electrical Engineering, North Minzu University, Yinchuan, China, in 2017, and the M.S. degree from the Department of Electrical Engineering, Hebei University of Science and Technology, China., in 2020. He is currently pursuing the Ph.D.degree in power electronics with the Hebei University of Technology, Tianjin, China.

His current research interests include dc–dc converter, electrical vehicles, and renewable power conversion system.

Yu Tang (Senior Member, IEEE) received the B.S. and the Ph.D. degree both from the Department of Electrical Engineering, Nanjing University of Aeronautics and Astronautics (NUAA), China, in 2003 and 2008, respectively. He joined the Electrical Engineering Department in NUAA since 2008 and State Key Laboratory of State Key Laboratory of Reliability and Intelligence of Electrical Equipment, Hebei University of Technology since 2018. He has published more than 80 papers in journals and conference proceedings. The research area includes power electronics in renewable energy generation.

Dr. Tang is the Guest Associate Editor of the IEEE Trans.on Power Electronics.

Zhe Zhang (Senior Member, IEEE) received the B.Sc. and M.Sc. degrees in power electronics from Yanshan University, Qinhuangdao, China, in 2002 and 2005, respectively, and the Ph.D. degree in power electronics from the Technical University of Denmark, Kgs. Lyngby, Denmark, in 2010.

From 2014 to 2021, he was an Associate Professor with the Department of Electrical Engineering, Technical University of Denmark (DTU), where he has been the Head of Studies in charge of Electrical Engineering M.Sc. Programme since January 2018.He has authored or co-authored more than 200 transactions and international conference papers and filed over 10 patent applications. Dr. Zhang was the recipient of the awards and honors, including Best Paper Awards in IEEE conferences of ECCE, IFEEC, and IGBSG, Best Teacher of the Semester, Chinese Government Award for Outstanding Students Abroad, etc. He is an Associate Editor for the IEEE Transactions on Industrial Electronics, IEEE Journal of Emerging and Selected Topics in Power Electronics, and IEEE Access, and Guest Editor for the IEEE Journal of Emerging and Selected Topics in Industrial Electronics.

Leijiao Ge (Senior Member, IEEE) received Ph.D. degree in electrical engineering from Tianjin University, Tianjin, China, in 2016. He is currently an associate professor in the school of electrical and information engineering at Tianjin University.

His main research interests are smart distribution network, cloud computing and big data.

Pooya Davari (Senior Member, IEEE) received the B.Sc. and M.Sc. degrees in electronic engineering, in2004 and 2008, respectively, and the Ph.D. degree in power electronics from QUT, Brisbane City, QLD, Australia, in 2013.

From 2005 to 2010, he was involved in several electronics and power electronics projects as a Development Engineer. From 2013 to 2014, he was with the QUT, as a Lecturer. He joined the Aalborg University (AAU), Aalborg, Denmark, in 2014, as a Postdoc, where he is currently an Associate Professor. He has authored/coauthored more than 180 technical papers. Dr. Davari served as a Guest Associate Editor of IET Journal of Power Electronics, IEEE Access Journal, Journal of Electronics, and Journal of Applied Sciences. He is an Associate Editor of Journal of Power Electronics and IET Electronics, and an Editorial board member of Journal of Applied Sciences and Journal of Magnetics. He is a member of the International Scientific Committee of EPE (ECCE Europe) and a member of Joint Working Group six and Working Group eight at the IEC standardization TC77A. He is the recipient of Equinor 2022 Prize and 2020 IEEE EMC Society Young Professional Award for his contribution to EMI and Harmonic Mitigation and Modeling in Power Electronic Applications. He is currently an Editor-in-Chief of Circuit World Journal. He is a Founder and a Chair of IEEE EMC Society Chapter Denmark and a Leader of EMI/EMC in Power Electronics Research Group at AAU Energy.